PCCP

ROYAL SOCIETY OF CHEMISTRY

PAPER

View Article Online
View Journal | View Issue



Cite this: *Phys. Chem. Chem. Phys.*, 2026, **28**, 7604

# Photothermal reshaping and cavity formation in silica-coated gold nanorods using nanosecond pulsed lasers

Tahani Albogami, [ab] Lucien Roach, [c] Sarah Alshehri, [abd] James McLaughlan, [e] Zabeada Aslam, [bf] Zhan Yuin Ong, [ab] Stephen D. Evans [ab] and Kevin Critchley [*ab]

The aspect ratio of Au nanorods can be precisely engineered using near-infrared nanosecond-pulsed laser irradiation, which enables ultrafast, confined energy deposition inaccessible under continuous-wave irradiation. In this study, we demonstrate a novel method for reshaping Au nanorods encapsulated within thin (<10 nm) silica shells. By leveraging the silica shell as a rigid nanocrucible, nanosecond laser irradiation induces rapid, end-selective shortening of the Au nanorod core, creating terminal cavities of a controllable size. Transmission electron microscopy confirms that while hexadecyltrimethylammonium bromide-coated Au nanorods convert into spherical and ϕ-shaped nanoparticles, the silica shell constrains the laser induced reshaping process, preserving the rod-like morphology while systematically reducing the aspect ratio. Consequently, the distinct longitudinal and transverse plasmon resonances are retained post-irradiation. The reshaping can be precisely controlled by adjusting laser fluence, resulting in a fine-tuned aspect ratio and a significantly narrowed longitudinal resonance, an outcome typically associated with femtosecond laser systems. 4D Scanning transmission electron microscopy reveals that the Au nanorods transform from single crystal to polycrystalline structures upon irradiation, providing direct evidence that nanosecond pulsed irradiation induces complete Au core melting and rapid recrystallization within the shell – with multiple nucleation sites. Despite the polycrystalline structure the resonance peak was narrower than that of the starting nanorod. This method for fabricating Au nanorods with integrated cavities within the offers significant potential for applications in triggered drug delivery, biosensing, and photoacoustic imaging.

Received 22nd January 2026,
Accepted 18th February 2026

DOI: 10.1039/d6cp00240d

rsc.li/pccp



## 1. Introduction

Au nanorods (AuNRs) are intensively investigated for applications in medical imaging and therapeutic applications, principally because of their strong, tunable, longitudinal surface plasmon resonance (LSPR) in the near-infrared (NIR) range.[1–4] Having an LSPR band in the NIR region enables AuNRs to be an effective material for analytical,[5–7] photofunctional,[8–11] diagnostic,[12] and biomedical photoacoustic applications.[1,13] Irradiating AuNRs at their LSPR dramatically elevates the electron temperature, which then dissipates *via* non-radiative pathways—chiefly electron–phonon and phonon–phonon coupling—producing heat and causing a rapid rise in the AuNR internal temperature.[12] It has been reported that the light-to-heat energy conversion can be up to 100% under particular conditions, such as when the absorption cross-section dominates over the scattering cross-section ($\sigma_{abs} \gg \sigma_{scat}$).[14] The scattering cross-section of Au nanoparticles scales with $D^6$, whereas the absorption cross-section scales with $D^3$, where $D$ is the particle diameter. Below $D \sim 50$ nm Au nanoparticles behave as pure absorbers, because their scattering cross-section is negligible compared to the absorption, while around $D \sim 100$ nm the cross-sections are comparable and above this scattering is the dominant effect.[12,14]

Rapid heating of the AuNRs induced by a pulsed laser can cause AuNRs to undergo reshaping, which leads to a reduction in aspect ratio (*AR*) and resulting in a blueshift or even loss of the LSPR band.[15–17] This reshaping behavior is influenced by several factors such as the starting *AR*, the surfactant types,

[a] *School of Physics & Astronomy, University of Leeds, LS2 9JT, UK. E-mail: k.critchley@leeds.ac.uk*
[b] *Bragg Centre, University of Leeds, LS2 9JT, UK*
[c] *CNRS, ENS de Lyon, Laboratoire de Chimie (LCH, UMR 5182), 69342, Lyon, France*
[d] *Department of Physics, College of Science, University of Bisha, P.O. Box 551, Bisha 61922, Saudi Arabia*
[e] *School of Electronic & Electrical Engineering, University of Leeds, LS2 9JT, UK*
[f] *School of Chemical & Process Engineering, University of Leeds, LS2 9JT, UK*

coating, the surrounding medium (water or organic), the laser types (femtosecond, nanosecond, or continuous wave), and the laser intensity.[9,15,16] When the heating rate is greater than cooling rate of AuNR lattice, there can be sufficient energy for surface atoms to break free and transition to a liquid state or, in more extreme cases, melting of whole AuNR can occur.[15,18] While reduction of a material's size is known to reduce the melting point, $T_m$, this is most pronounced when the nanoparticle approaches a few nanometers, therefore, for the majority of reported AuNRs studied, the melting point of Au is close to the bulk value.[18,19] However, reshaping does not require the melting temperature of the AuNR to be reached, it only requires that the surface atoms are sufficiently mobile. This phenomenon has been simulated for silver nanoparticles and AuNRs where there is a critical temperature, $T_S$, above which the 'surface' of a nanoparticle can effectively melt and become liquid-like below the melting point, $T_m$, of the material.[16,20–22] Recent *in situ* studies have provided significant insight into the thermal reshaping of acicular Au nanoparticles, demonstrating that at moderate temperatures, the process is governed by a slow, two-step surface diffusion of Au atoms from the tips to the body.[23] When $T_S < T < T_m$ the surface atoms are mobile and reshaping will occur to minimize the Gibbs free energy of the particle. This also implies that higher *AR* AuNRs will be less thermodynamically stable and may undergo faster reshaping.

The type of excitation source employed (pulse and width) is important for the photothermal reshaping.[4,9,15] Link *et al.* reported that nanosecond-pulsed laser sources the caused AuNR fragmentation at high fluences ($>4$ J cm$^{-2}$), while at lower fluences the AuNRs where quickly melted into nanospheres.[15] At a lower fluence of 0.64 J cm$^{-2}$, nanosecond-pulsed laser sources reportedly produced partial melting resulting in AuNRs with bent and twisted shapes. Low fluence nanosecond-pulsed lasers do not seem to cause surface-type melting, while femtosecond-pulsed lasers can lead to shorter *AR* AuNRs.[15] Link *et al.* reported that the threshold fluence for complete melting is nearly two orders of magnitude lower for femtosecond laser pulses compared with nanosecond laser pulses.[15] Laser reshaping blueshifts the AuNR LSPR peak and significantly impacts the efficacy of AuNRs for photothermal conversion (or photoacoustic contrast) as the peak AuNR absorbance rapidly moves away from the incident laser wavelength.[7,24] Therefore, to understand and control the degree of laser-induced reshaping is an important step in realizing AuNRs for many laser-based applications.

Experimental studies show that organic coatings, such as CTAB, can have an impact on the reducing or modifying the nature of the reshaping.[25] Furthermore, inorganic coatings such as silica are widely used to enhance the photothermal stability of AuNRs by a post-synthesis modification, and this remains an active area of research. For instance, slow thermal annealing has been used to tune the LSPR of both CTAB-stabilized and silica-shelled AuNRs by physically reshaping the core.[26] However, this process relies on equilibrium heating, which differs fundamentally from the rapid, non-equilibrium conditions induced by high-fluence laser pulses. In another study, Au nanoworms where synthesized and coated in silica and exposed to a nanosecond pulsed laser.[27] This exposure resulted in a blue-shift in the LSPR that was dependent on the fluence. While the blueshift suggests a reduction in aspect ratio (*e.g.*, similar to the AuNRs), the mechanism and morphology of the Au nanoworms was not fully investigated.[27] Khanadeev *et al.* showed increased photostability of Au nanorods that are coated in silica to nanosecond pulsed laser irradiation.[28] Shells of increasing thickness (*e.g.* from 24 to 57 nm) were found to enhance photostability.

The potential to harness nanosecond-pulsed laser-induced morphological changes of the AuNRs within thin protective shells remains largely unexplored. The aim of our work is to address this gap by providing a detailed investigation into how nanosecond-pulsed laser excitation can be used to controllably reshape CTAB-stabilized AuNRs encapsulated in a thin silica shell. By pinpointing the laser conditions that transform the rod-like core into a more spherical shape, we demonstrate a novel, physical method for engineering hybrid nanostructures with well-defined internal cavities. This laser-based approach presents a compelling alternative to established fabrication routes for such 'void-space' structures, which often rely on complex chemical steps like the selective oxidation of sacrificial layers.[29–31] The ability to create these voids on-demand could unlock unique applications for these materials as nanoreactors, advanced drug delivery vehicles, or highly sensitive plasmonic sensors.

## 2. Materials and methods

### 2.1. Materials

Gold(III) chloride trihydrate (520918), hexadecyltrimethylammonium bromide (CTAB, H6269), sodium oleate (233978), sodium borohydride (452882) and tetraethyl orthosilicate (TEOS, 78-10-4) were purchased from Sigma-Aldrich. Silver nitrate (11414), hydrochloric acid (12.1 M, UN1789) and ethanol (E/0650DF/17) were purchased from Fisher Scientific. Ascorbic acid (A15613) was purchased from Alfa Aesar. Methanol (20847) was purchased from VWR. All chemicals were used as received without any additional purification. Deionized water was supplied using a Milli-Q system (resistivity of 18.2 MΩ cm).

### 2.2. AuNR synthesis

*Aqua regia* was used to clean glassware. The AuNRs were synthesized using seedless synthesis method that was developed by Roach *et al.*[32,33] to obtain AuNRs with *AR* of ~4.0, the following conditions were applied. First, an aqueous binary surfactant solution consisting of 4 mL of CTAB solution (40 mM), 1.25 mL of sodium oleate solution (12.5 mM) and 4.75 mL of water was prepared. This was followed by the addition of 10 mL of gold(III) chloride trihydrate solution (1 mM), 480 μL of silver nitrate solution (4 mM), 100 μL hydrochloric acid (11.8 M), 150 μL ascorbic acid solution (85.8 mM). The orange color disappeared after the addition of the ascorbic acid, resulting from the reduction of $Au^{3+}$ to $Au^{+}$. Finally, 15 μL of freshly prepared ice-cold sodium borohydride solution (10 mM) was

injected rapidly into the mixture. The reaction was maintained at 30 °C for 4 h to allow the reaction to complete. The color of the solution turned to a reddish-brown color. The resulting AuNR suspension was centrifuged at 17000 × *g* for 30 min. The precipitate was isolated and then resuspended in 10 mL water and stored at room temperature and in the dark. These samples are referred to as AuNRs@CTAB for short, despite the surface composition being a mixture of CTAB and sodium oleate.

### 2.3. Coating the AuNRs with Silica

A modified version of the method described by Ashrafi *et al.* was used to encapsulate the AuNRs in silica.[34] To remove any aggregated AuNRs, 10 mL of the cleaned AuNR suspension (at 50 μg $mL^{-1}$) were centrifuged at 500 × *g* for 3 min and the supernatant is collected. Then 20 μL of 0.1 M NaOH solution was added to AuNR suspension to adjust the pH to 10. The solution was left for 30 min while being gently stirred. A methanol solution of TEOS 20% (v/v) was prepared. Three injections of the TEOS solution, separated by 30 min intervals were added to the AuNR suspension (30 μL TEOS solution per 1 mL of AuNR suspension). The reaction was maintained at a temperature of (27 ± 1) °C, left continuously stirred for 3 days. The silica-coated AuNRs (AuNRs@$SiO_2$) were centrifuged multiple times (8000 × *g*, 10 min) and resuspended in 10 mL of deionized water and kept in the dark at room temperature. These samples are referred to as AuNRs@$SiO_2$ from hereon. The porosity of the $SiO_2$ shells was estimated spectroscopically (see Section S1 in the SI).[35]

### 2.4. Finite element method (FEM) simulations

The optical responses of the AuNRs were simulated using COMSOL's radio frequency module. Calculations were performed in the frequency domain in the scattered field formulation using the PARDISO direct solver. Refractive index values for Au were taken from Johnson and Christy.[36] Particles were simulated embedded in a medium of water ($n$ = 1.33) surrounded by a perfectly matched layer. The AuNRs were modeled as a cylinder capped by ellipsoidal hemispheres of independently tunable geometry. The silica shell ($n$ = 1.45) was modelled as a larger cylinder capped by ellipsoidal hemispheres. The geometry was chosen to create a shell of constant thickness. A cavity was included in the interior of some of the structures. $\sigma_{abs}$ was calculated through a volume integral of the resistive heat losses inside the particle, $Q_{rh}$. $\sigma_{scat}$ was calculated through a surface integral of the Poynting vector at the particle surface. For 'angular-averaged' spectra and field maps the polarization of the light was oriented at an angle of $\cos^{-1}(1/\sqrt{3}) \sim 54.7^\circ$ from the long axis of the AuNR. This angle corresponds to the well-known 'magic angle', defined by the condition $\cos^2\theta = 1/3$. At this angle, second-rank tensor (dipolar) interactions are averaged in the same way as for a full orientational average, which ensures that the relative weighting of longitudinal and transverse dipole contributions matches the true angular average. This follows directly from the standard treatment of dipolar anisotropy.[37]

For the simulation of heat generation COMSOL's Heat Transfer module in the time domain was used as second-simulation step following the optical simulation. An optical simulation was run at the wavelength and intensity of the laser at peak pulse power and the calculated $Q_{rh}$ for these conditions was used a heat source. Hence, this simulation assumes that the laser has an infinitely narrow spectral bandwidth. This is not a major inaccuracy due to the spectral linewidth of a laser being significantly narrower than the typical AuNR LSPR peak. To give the corresponding time profile for $Q_{rh}$, it then was multiplied through by a normalized Gaussian pulse of form,

$$f(t) = \frac{2}{w}\sqrt{\frac{\ln 2}{\pi}}\exp\left\{-4\ln 2\frac{(t-t_0)^2}{w^2}\right\} \quad (1)$$

where $w$ is the pulse width and $t_0$ is the pulse center. Providing a heating pulse which is Gaussian in time and the correct peak intensity. Temperature distributions were then be recovered from point probes along a single axis. Simulations were ended before a significant amount of the generated heat could leave the simulated region. The upper time limit over which these calculated temperature distributions will be physical is given by the thermal diffusion time, $\tau_{th} = r^2/\alpha$, where $r$ is the shortest distance between the particle and the boundary of the simulation and $\alpha$ is the thermal diffusivity ($\alpha = 1.43 \times 10^{-7}$ $m^2$ $s^{-1}$ for water). It should be noted that there are number of limitations to these simulations. Phase changes were not accounted for, and the corresponding changes in the thermal and optical properties entailed by these. The simulations also assume an ultranarrow width to the spectrum of the illumination source.

### 2.5. Characterization

**2.5.1. UV-vis-NIR extinction spectroscopy.** The UV-vis-NIR extinction spectra in this study were recorded using an Agilent Cary 5000 UV-vis-NIR extinction spectrometer. Quartz crystal cuvettes were used for all solution-based samples ($L_{path}$ = 1 cm). All measurements were performed at room temperature (~21 °C).

**2.5.2. Transmission electron microscopy.** The size and shape of the AuNRs were investigated using TEM of the synthesized AuNRs, using an FEI Tecnai TF20 microscope with an acceleration voltage of 200 kV. The samples were prepared by drying 2 μL of AuNR dispersion on TEM grids. The end-cap geometry of the AuNR is defined by:

$$e = \frac{2a}{D} \quad (2)$$

where $a$ is the longitudinal semi-axis of the ellipsoid defining the tip, and $D$ is the AuNR diameter as recommended in reference.[38] *AR* is defined by $L/D$, where $L$ is the total length of the AuNR.

**2.5.3. Scanning transmission electron microscopy.** Scanning transmission electron microscopy (STEM) was used for measuring the AuNR morphology and structures. The STEM images were obtained using a Tescan Tensor microscope operated at an acceleration voltage of 100 kV. The samples were prepared by depositing 15 μL of the AuNRs@$SiO_2$

 

suspension on to a 400-mesh carbon-coated copper grid and left to dry. Data acquisition and data processing were carried out using the Tensor Explore software. The diffraction patterns were collected with a beam current of 250 pA and a convergence semi-angle of 2 mrad; the diffraction pattern field of view was 80 mrad. Structure files (fcc Au from the Crystallography Open Database, ID 1545302)[39] were used to generate templates for matching to the acquired diffraction patterns.

### 2.6. Nanosecond-pulsed laser irradiation of AuNR samples

The nanosecond-pulsed laser irradiation of AuNRs@CTAB and AuNRs@$SiO_2$ aqueous dispersions, at concentrations of 50 μg $mL^{-1}$, was investigated using a tunable optical parametric oscillator laser system (Vibrant, OPOTEK, Inc.) at a wavelength of 850 nm (unless stated otherwise). The beam had a pulse width of 7 ns, a repetition frequency of 10 Hz, and a beam diameter of ~6 mm. A quartz cuvette was filled with the aqueous dispersion of the AuNRs@CTAB and AuNRs@$SiO_2$ particles, which was then continuously stirred with a magnetic bar during pulsed laser irradiation for various exposure times (typically 5 min). The starting temperatures of the aqueous solutions were room temperature (~21 °C).

## 3. Results

### 3.1. Characterization of the AuNRs@$SiO_2$ nanoparticles

The optical and morphological properties of the as-synthesized, CTAB-stabilized AuNRs (AuNR@CTAB) were characterized prior to silica coating. UV-vis-NIR extinction spectroscopy revealed two distinct absorption bands (Fig. 1a): a transverse surface plasmon resonance (TSPR) at 511 nm and a LSPR at 830 nm, confirming the anisotropic shape. TEM analysis (Fig. 1b) corroborated this, showing rod-shaped particles with an average length of (47 ± 9) nm, a diameter of (12 ± 2) nm, and a corresponding *AR* of (3.9 ± 0.8) ($N$ = 100, see Fig. S2 in the SI). Successful encapsulation of these AuNRs within a uniform silica shell was confirmed by TEM (Fig. 1c), which showed a mean shell thickness of (6.8 ± 0.2) nm. The optical signature of this coating process was a predictable redshift of the LSPR peak to (836 ± 1) nm. This shift is the expected consequence of increasing the local refractive index at the Au-dielectric interface upon silica deposition, as reported elsewhere.[3] The LSPR peak was also slightly broadened, with the full-width half-maximum (FWHM) increasing from 174 to 204 nm. The coating caused the TSPR peak to be shifted by only 2 nm. These final hybrid particles are hereafter referred to as AuNRs@$SiO_2$.

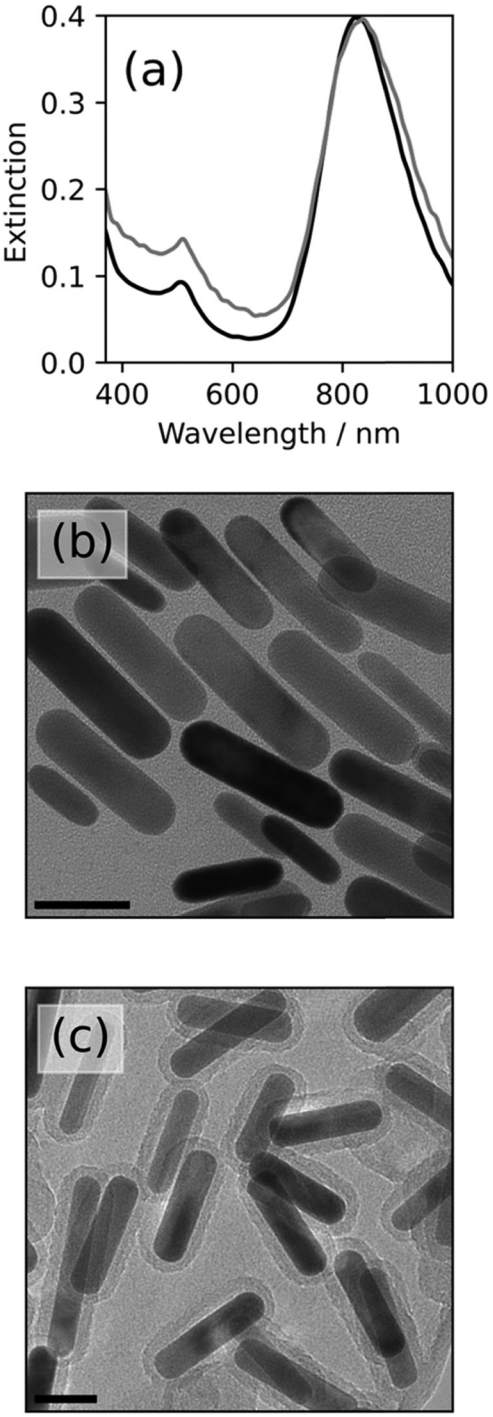


Fig. 1 (a) UV-vis-NIR extinction spectra of AuNRs@CTAB (black) and AuNRs@$SiO_2$ (grey). TEM micrographs of (b) AuNRs@CTAB and (c) AuNRs@$SiO_2$ samples. All scale bars are 25 nm.

### 3.2. Nanosecond-pulsed laser irradiation of AuNRs and AuNRs@$SiO_2$

To investigate the effect of the silica shell on photothermal reshaping, AuNRs@CTAB and AuNRs@$SiO_2$ solutions were irradiated using a nanosecond-pulsed laser ($\lambda$ = 850 nm) at fluences of 20 and 10 mJ $cm^{-2}$. The resulting morphological changes were monitored in real-time by observing the evolution of the LSPR and TSPR bands, which are highly sensitive to the *AR*.

**AuNRs@CTAB.** Upon irradiation at 20 mJ $cm^{-2}$, the uncoated AuNRs@CTAB exhibited a rapid and total transformation (Fig. 2a). Within 30 s, the longitudinal LSPR band at 832 nm was completely extinguished. Concurrently, the TSPR band intensified and redshifted from 511 nm to 522 nm. This

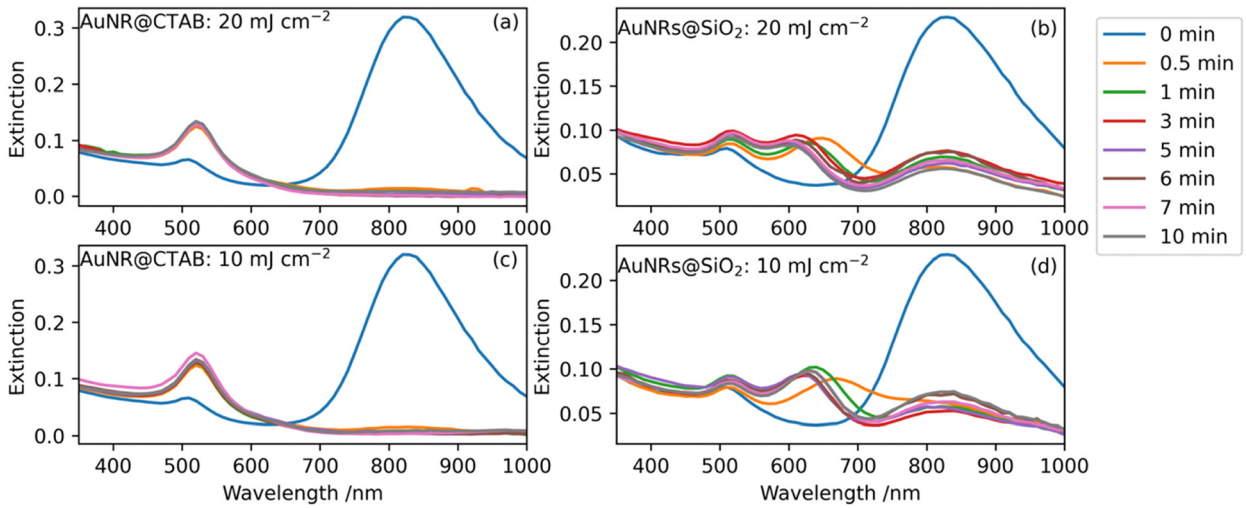


Fig. 2 UV-vis-NIR extinction spectra of the two AuNR samples before and after pulsed laser irradiation (up to 10 min), with a wavelength of 850 nm. The pulsed laser, with a fluence of 20 mJ cm$^{-2}$ irradiated solutions containing (a) AuNRs@CTAB and (b) AuNRs@SiO$_2$ nanoparticles. A lower laser fluence of 10 mJ cm$^{-2}$ was used to irradiate (c) AuNRs@CTAB and (d) AuNRs@SiO$_2$ samples.

spectral signature—the disappearance of the LSPR band and the emergence of a single plasmon band characteristic of the AuNRs melting and reshaping into nanospheres. Nearly identical spectral changes were observed at the lower fluence of 10 mJ cm$^{-2}$ (Fig. 2c), indicating that the energy threshold for complete melting was surpassed in both cases.

**AuNRs@SiO$_2$.** In contrast, the reshaping of the AuNRs@SiO$_2$ appear to have had their Au cores physically constrained by the silica shell. When irradiated at 20 mJ cm$^{-2}$ (Fig. 2b), the original LSPR band at 830 nm rapidly decreased in magnitude but, crucially, did not disappear entirely. Instead, a new, distinct LSPR band emerged at a blue-shifted wavelength of ~654 nm, which continued to blueshift to ~611 nm with prolonged exposure. This behavior signifies a transformation from the initial high *AR* nanorods into a population of shorter, lower *AR* rods confined within the rigid silica shell. The TSPR band showed only a minor increase in magnitude and a slight redshift (513 nm to 517 nm), further supporting that the particles remained anisotropic. A weaker peak centered around 830 nm persisted suggesting that a small fraction of the AuNRs have maintained their *AR*.

At the lower fluence of 10 mJ cm$^{-2}$ (Fig. 2d), the AuNRs@SiO$_2$ followed a similar reshaping pathway but with less slightly less strength. The new LSPR band appeared at a slightly longer wavelength (665 nm) with its final position was also less blue shifted (621 nm), suggesting that the degree of reshaping is fluence-dependent.

TEM (Fig. 3a–c) was used to examine the form and morphological changes of the AuNRs@CTAB after 0 min, 1 min, and 5 min of nanosecond-pulsed laser exposure (850 nm, 20 mJ cm$^{-2}$). After 1 min of pulsed laser irradiation, the AuNRs@CTAB noticeably transition from a nanorod morphology to spherical, ellipsoidal, or "ϕ" shapes (Fig. 3b), consistent with previous reports.[15] Spherical and ϕ-shaped AuNRs were the most frequently found particles, with yields of 35% and 32%, respectively ($N$ = 100). Approximately, 18% of the AuNRs retained their original shapes after pulsed laser irradiation. The remaining 14% of the particles were lower *AR* AuNRs. The remaining AuNRs had $AR_{1\,min} = 2 \pm 1$ and $e_{1\,min} = 1.4 \pm 0.4$ after 1 min of exposure; and $AR_{5\,min} = 1.3 \pm 0.6$ and $e_{5\,min} = 1.3 \pm 0.4$ after 5 min of exposure.

The morphological evolution of the AuNRs@SiO$_2$ particles under laser irradiation (850 nm, 20 mJ cm$^{-2}$) was also characterized by TEM (Fig. 3d–f). In contrast to the uncoated particles, the silica shell maintained the Au core with an anisotropic shape. The shell acted as a rigid nanoscale crucible, confining the AuNR reshaping process. A key consequence of this confined reshaping is the creation of a void within the shell. As the AuNR core melted and contracted to a lower *AR*, it pulled away from the silica wall, resulting in a distinct cavity, typically at one end (~92%), but occasionally at both ends of the metallic core. After 5 min of irradiation most of the intact core–shell particles exhibited a well-defined single internal cavity. The reshaping process produced a heterogeneous population of Au core morphologies (Fig. 3f), *e.g.*, 57% of the cores retained a rod-like shape (though with a lower *AR*), 30% adopted a distinct dumbbell-like morphology, and the remaining 13% were irregular. This reshaping was also accompanied by a change in the end-cap geometry, with the tips of the cores transitioning from a nearly hemispherical shape to a more pointed, prolate form ($e > 1$). A small fraction of particles appeared unaffected by the laser, and in some instances, the silica shell was observed to have fractured, leaving an empty shell.

Statistical analysis of the TEM images provides quantitative insight into the different reshaping mechanisms for the AuNRs@SiO$_2$ and AuNRs@CTAB (Fig. 4). For the AuNRs@CTAB, the size distributions confirm a rapid and complete melting into near-spherical particles. Before irradiation, the length, diameter, and *AR* distributions were relatively narrow (Fig. 4a–c). After just 1 min of laser exposure, the length

 

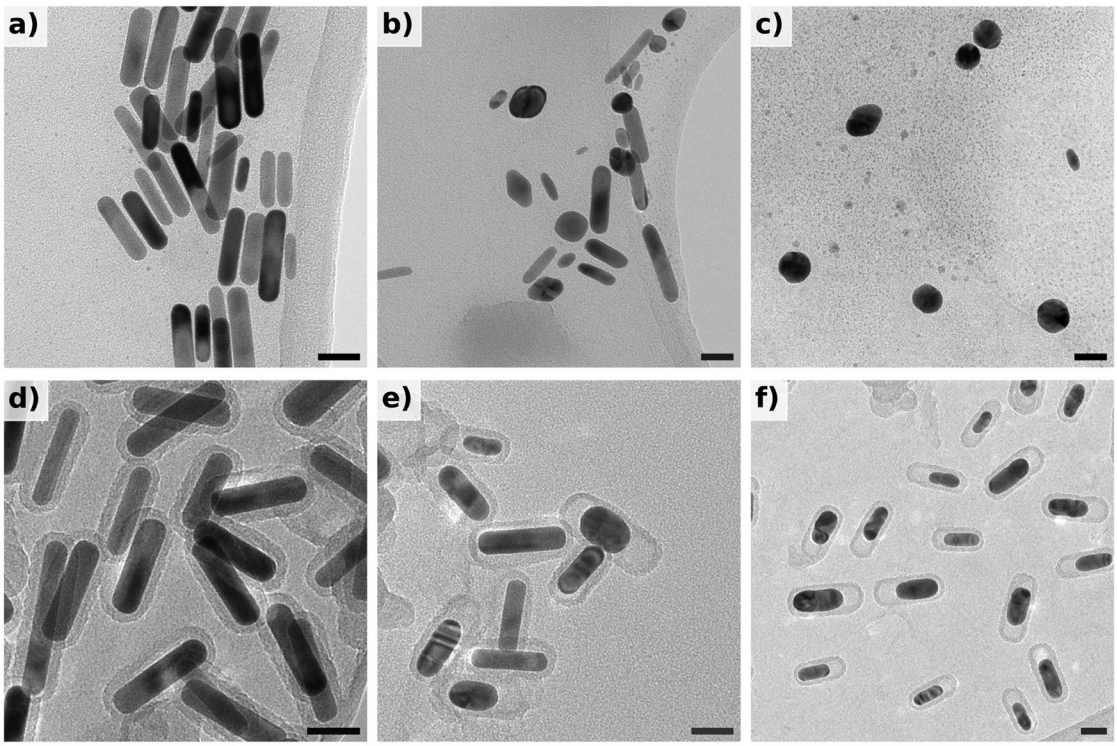


Fig. 3 TEM images of AuNRs before and after nanosecond-pulsed laser irradiation ($l$ = 850 nm) with a fluence of 20 mJ cm$^{-2}$. AuNRs@CTAB samples irradiated for (a) 0 min, (b) 1 min, and (c) 5 min. AuNRs@$SiO_2$ samples irradiated for (d) 0 min, (e) 1 min, and (f) 5 min. The scale bars represent 25 nm.

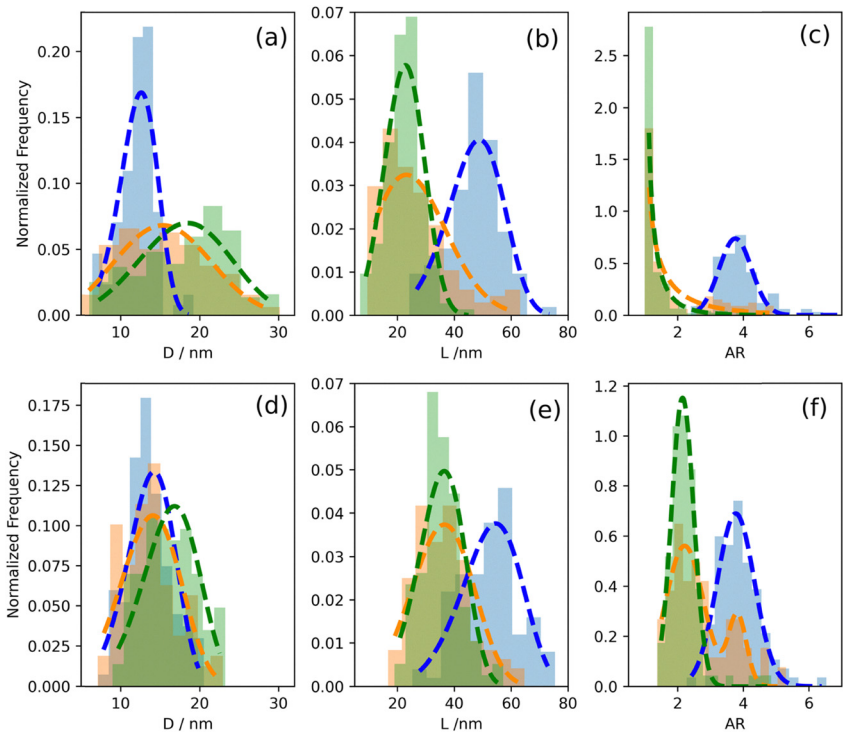


Fig. 4 Histograms of the AuNR core geometry of the AuNRs@CTAB (a)–(c) and AuNRs@$SiO_2$ (d)–(f) samples before and after pulsed irradiation (850 nm, 20 mJ cm$^{-2}$). The histograms of the AuNR core diameters, $D$ (a) and (d); lengths, $L$ (b) and (e); and AR (c) and (f) for 0 min (blue), 1 min (orange), and 5 min (green). The dashed lines are the corresponding lines of best fit to Weibull distribution functions ($N > 100$).

distribution shifts dramatically to shorter values while the diameter distribution broadens and shifts to larger values. This collapse results in a population with a mean *AR* of ~2. Continued exposure to 5 min appears to reduce the *AR* further to slightly narrow these final distributions, suggesting the system settles into a more uniform, thermodynamically stable state.

In contrast, the AuNRs@$SiO_2$ samples show a distinctly different reshaping pathway that is physically constrained by the shell. After 1 min of irradiation at 20 mJ $cm^{-2}$, the *AR* distribution is clearly bimodal: it contains a population of untransformed rods retaining their original *AR* (~3.9), alongside a new population of reshaped AuNRs with a mean *AR* of 2.2 ± 0.6. With continued exposure for 5 min, the initial population was fully depleted, resulting in a single, narrower distribution centered at a final mean *AR* of 2.2 ± 0.3 (Fig. 4f). The end-cap geometry of the rod before irradiation the caps are slightly oblate-hemispherical ($e < 1$), but after 5 min irradiation it shifts to a slightly prolate hemispherical ($e > 1$). Crucially, the reduction in *AR* was found to be fluence-dependent. A separate sample irradiated at a lower fluence of 10 mJ $cm^{-2}$ followed the same pathway, but the extent of reshaping was less pronounced. After 5 min, the final mean *AR* was 2.8, significantly higher than the 2.2 achieved at the higher fluence (Fig. S3 in the SI). This demonstrates that within the silica shell, the final morphology of the Au core is not only controlled but is also tunable by adjusting the incident laser power. Interestingly, the analysis also revealed subtle changes in the silica shell's morphology after five min of irradiation at 20 mJ $cm^{-2}$. The hybrid nanoparticles total mean length and mean width slightly increased from 57 nm and 22 nm to 60 nm and 26 nm, respectively. However, the shell thickness was observed to decrease slightly by 1.2 nm (Table 1), this could be possibly explained by condensation of the silica shell because of the photothermal heat generation, although this requires further characterization to be stated definitively. The main parameters are summarized in Table 1.

Nanosecond-pulsed laser irradiation of AuNRs@$SiO_2$ nanoparticles induces a controlled reshaping of the Au core within the silica shell, rather than fragmentation or disintegration. This conclusion is supported by basic volumetric calculations, detailed elemental mapping and scanning transmission electron microscopy (STEM) image analysis (see Sections S4 & S5 in the SI, respectively). Based on the analyses provided, laser irradiation of AuNRs@$SiO_2$ nanoparticles induces a controlled reshaping of the Au core within the silica shell, rather than fragmentation or disintegration. This conclusion is supported by detailed elemental mapping, TEM image analysis, and volumetric calculations. Evidence against fragmentation comes from a volumetric analysis of the Au cores before and after laser exposure. By applying thresholding techniques and contour fitting algorithms to TEM images, the 2D shapes of hundreds of AuNR cores were converted into binary images and extrapolated into 3D volumes. The mean volume of the Au cores was found to be approximately the same before and after irradiation at 20 mJ $cm^{-2}$, a result consistent with a process of melting and recrystallization contained within the silica shell (Fig. S4 in the SI).

This finding was further corroborated by elemental mapping. Energy-dispersive X-ray (EDX) spectroscopic maps of the AuNRs@$SiO_2$ structures show no evidence of Au dispersion or fragmentation outside of the Au core region after 5 min of laser irradiation (Fig. S5 in the SI). The EDX maps provide insight into the behavior of the CTAB surfactant layer. Before irradiation (Fig. S6 in the SI), signals for N and Br overlap with the Au, consistent with the presence of CTAB. Following irradiation, the Br signal becomes weaker and is only present in the region of reshaped Au core, suggesting a possible partial removal or degradation of the CTAB, though this cannot be definitively confirmed from the EDX data alone.

While the Au cores remain intact, they undergo significant morphological changes. To systematically categorize the diverse shapes produced by the reshaping process, the binary images derived from TEM analysis were processed using an unsupervised 16-layer hierarchical clustering model. This computational approach successfully classified the post-irradiation morphologies into four primary types (Fig. S7 in the SI): (a) nanorods: particles that retained their general rod shape, albeit often with a lower *AR*; (b) irregular rods: elongated particles that lost their uniform cylindrical shape; (c) ovoids: particles that collapsed into more spherical or egg-like shapes; and (d) dumbbell-like: particles exhibiting a distinct, pinched-in center.

### 3.2. Simulation of AuNRs@$SiO_2$ extinction spectra

In Fig. 5a, FEM simulated spectra are shown for the AuNRs in Fig. 1 (also Fig. S8 in the SI), before and after photothermal reshaping by a 5 mJ $cm^{-2}$ laser pulse. The respective AuNR@$SiO_2$ dimensions used were ($L$ = 55 nm, $D$ = 14.5 nm, $e_1 = e_2 = 0.6$) before and ($L$ = 48 nm, $D$ = 17 nm, $e_1$ = 0.6, $e_2$ = 0.92) after reshaping, with a silica thickness of $t$ = 6 nm. After reshaping, the

Table 1 The mean dimensions of AuNRs@CTAB and AuNRs@$SiO_2$ samples before and after nanosecond-pulsed laser exposure (850 nm, 20 mJ $cm^{-2}$) as determined from analysis of TEM images and UV-vis-NIR spectroscopy. All values are given in the form (mean ± standard deviation)

| Sample | Exposure time (min) | $L$ (nm) | $D$ (nm) | *AR* | End-cap factor, $e$ | Silica thickness (nm) | LSPR (nm) | TSPR (nm) |
|---|---|---|---|---|---|---|---|---|
| AuNRs@CTAB | 0 | 47 ± 9 | 12 ± 3 | 3.9 ± 0.6 | 0.8 ± 0.2 | — | 832 ± 2 | 511 |
| AuNRs@CTAB | 1 | 26 ± 12 | 16 ± 6 | 2 ± 1 | 1.1 ± 0.3 | — | — | 522 |
| AuNRs@CTAB | 5 | 22 ± 6 | 18 ± 6 | 1.4 ± 0.7 | 1.1 ± 0.3 | — | — | 522 |
| AuNRs@$SiO_2$ | 0 | 50 ± 11 | 14 ± 3 | 3.9 ± 0.8 | 0.8 ± 0.1 | 6.8 ± 1.4 | 836 ± 2 | 513 |
| AuNRs@$SiO_2$ | 1 | 36 ± 10 | 14 ± 4 | 3 ± 1 | 1.0 ± 0.2 | 5.5 ± 0.9 | 624 ± 2 | 516 |
| AuNRs@$SiO_2$ | 5 | 35 ± 8 | 16 ± 4 | 2.2 ± 0.3 | 1.3 ± 0.2 | 5.6 ± 1.1 | 611 ± 2 | 517 |

 

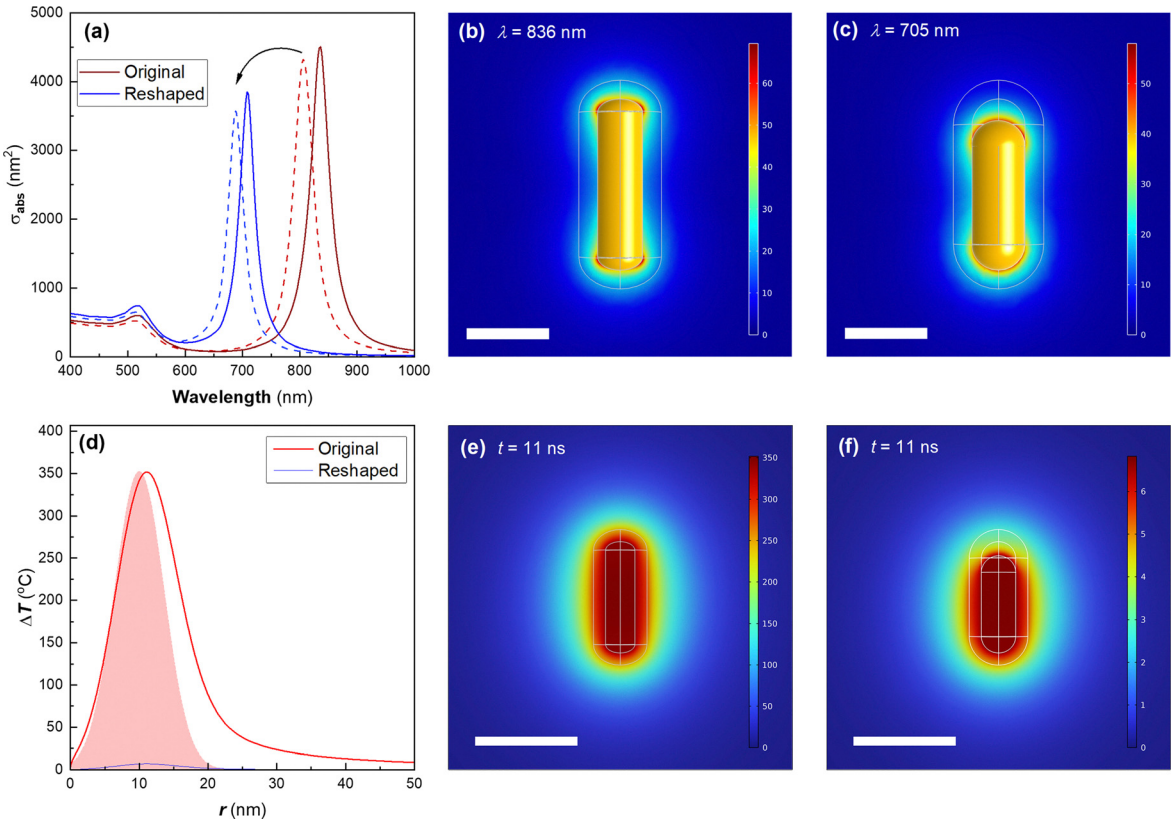


Fig. 5 Finite element modelling simulations of the electromagnetic and thermal responses of an AuNR@$SiO_2$ before and after reshaping. The respective dimensions used were ($L$ = 55 nm, $d$ = 14.5 nm, $e_1 = e_2$ = 0.6) and ($L$ = 48 nm, $D$ = 17 nm, $e_1$ = 0.6, $e_2$ = 0.92) before and after reshaping respectively with a silica thickness, $t$ = 6 nm. (a) Simulated absorbance spectra of AuNRs@$SiO_2$ particles (angular-average). The dashed lines are the spectra of the AuNR cores without a $SiO_2$ coating. Electric field enhancement maps ($E/E_0$) for (b) an original AuNR@$SiO_2$ at $\lambda$ = 836 nm and (c) a reshaped AuNR@$SiO_2$ at $\lambda$ = 705 nm under longitudinal excitation. The scale bar for (b) and (c) is 25 nm. (d) Temperature of the AuNR core of both AuNR@$SiO_2$ particles illuminated by a 5 mJ cm$^{-2}$, 850 nm, 7 ns laser pulse centered on $t$ = 10 ns as a function of time under longitudinal excitation. The profile of the laser pulse is shown as the shaded area. The full temperature distribution curves around the particle are given in Fig. S10 and S12 in the SI. (e) Temperature map of the original AuNR@$SiO_2$ at $t$ = 11 ns (1 ns after the peak of the laser pulse). (f) Temperature map of the reshaped AuNR@$SiO_2$ at $t$ = 11 ns. The scale bar for (e) and (f) is 25 nm.

geometry of the core AuNR was assumed to asymmetric with different end cap geometries ($e_1$ = 0.79 in contact with the $SiO_2$ and $e_2$ = 1.14 inside the cavity, *e.g.*, more prolate). The values of $\sigma_{abs}$ are the angular-averaged values. For the untreated sample, the predicted LSPR peak was at 836 nm ($\sigma_{abs}$ = 4505 nm$^2$), which closely matches the observed experimental LSPR band peak wavelength in Fig. 1a. By comparison, the reshaped geometry with an internal cavity (7 nm in length) had a predicted LSPR peak at 708 nm ($\sigma_{abs}$ = 3848.7 nm$^2$) this compares less favorably with the observed experimental LSPR peak wavelength of 610 nm. The electric field enhancement at the LSPR peak wavelength for each geometry is shown in Fig. 5b and c. The field enhancement of the original AuNR@$SiO_2$ is almost entirely restricted to within the silica shell coating the AuNRs, whereas in the reshaped case there is high field enhancement close to the AuNR tip inside the formed cavity. The calculations here predict a strong local field enhancement, $|\bar{E}/\bar{E}_0| \sim 55$, within the cavity of the AuNR@$SiO_2$ particle, enabling plasmonic enhancement of Raman scattering. Hence, molecules located within the cavity could be directly measured through Raman spectroscopy.

In addition to the optical simulations, computational modelling of the heat generated by a single laser pulse was also performed (Fig. 5d–f and Fig. S9–S17 in the SI). In these models, the laser polarization was aligned perfectly to the longitudinal axis of the AuNRs (*i.e.* the most efficient illumination configuration). This was assumed to be the most relevant scenario because, for all practical purposes, all AuNRs will experience pulses with close alignment to the light polarization multiple times. The short tumbling time of the particles ($\tau_r \sim 1$ μs), compared to the period of the laser pulse (= 100 ms), and the short width of the pulses ($\tau_p$ = 7 ns) particles will essentially be illuminated at a random angle during each pulse. Over 3000 pulses, there is a near certainty that the AuNR will be aligned to the polarization of the light source multiple times.

It can be seen in the electromagnetic simulations that there is precipitous drop in $\sigma_{abs}$ at the laser wavelength (850 nm) after reshaping from 2929 nm$^2$ to 58 nm$^2$, a 98% reduction, which reduces photothermal heat generation to comparatively very low levels. This can be seen in the simulations of the resulting heat generation. The original AuNR@$SiO_2$ particle upon

illumination by a pulse with characteristics: $\tau_p$ = 7 ns, $\lambda$ = 850 nm, and fluence = 5 mJ cm$^{-2}$ generates a peak temperature increase of $\Delta T$ = 352 °C, 1 ns after the peak of the laser pulse. Strong temperature gradients are generated for around 11 ns (the pulse is centered on 10 ns) before rapidly dissipating over the following 40 ns of the simulation (Fig. S10 and S17 in the SI). By comparison, the reshaped AuNR@$SiO_2$ particle only generates a peak temperature increases of $\Delta T$ = 7 °C (*i.e.* ~98% less, consistent with the drop in $\sigma_{abs}$). The temperatures achieved by the reshaped AuNR@$SiO_2$ particle are unlikely to result in any further morphological changes. By comparison, the temperatures achieved by the original AuNR@$SiO_2$ are hot enough to decompose organics. The highest predicted temperature increase at the silica-water interface is $\Delta T$ = 286 °C, which is close to the known threshold for bubble cavitation ($0.8T_{c,H_2O}$ ~ 300 °C),[40] given the ambient temperature of 20 °C. Hence, for higher pulse fluences we might expect consistent generation of cavitation events.

In addition, simulations were performed of the geometries seen in Fig. 3 which were exposed to a high pulse fluence of 20 mJ cm$^{-2}$ (Fig. S13–S17 in the SI). Similar trends can be seen with a ~99% drop in $\sigma_{abs}$ at 850 nm after reshaping. The LSPR of the original AuNR@$SiO_2$ (810 nm) is worse matched to the laser wavelength that in the previous case $\sigma_{abs}$ (850 nm) = 747 nm$^2$ (*vs.* 2929 nm$^2$ previously), hence despite a fourfold increase in laser pulse fluence, the peak temperature is roughly the same. After reshaping the heat generation at 850 nm would not be expected to induce any further changes in morphology.

### 3.4. Controlled reshaping *via* off-resonance excitation

To achieve more precise control over the reshaping process, the effects of off-resonance laser excitation was investigated. For this experiment, the AuNRs@$SiO_2$ were synthesized with a slightly lower *AR* to give a LSPR of ~800 nm. These particles were then irradiated with a nanosecond-pulsed laser at a fixed wavelength of 850 nm—intentionally above the LSPR peak—for a duration of 5 min (*i.e.*, 3000 pulses), at different fluences. Fig. 6a shows the UV-vis-NIR extinction spectrum, demonstrating a highly controllable, fluence-dependent reshaping of the Au cores. Before irradiation the LSPR maxima was at 800 nm and had a FWHM of 164 nm. Pulsed laser irradiation for 5 min resulted in a blueshift of the maxima which increased with increasing laser fluence. The experiment was repeated with a fresh AuNRs@$SiO_2$ sample, and the combined results are summarized in Fig. 6b. The LSPR band blueshifts and the FWHM values were found to decreased as a function of fluence (Fig. 6b). This confirms that by operating in an off-resonance regime, the final *AR* of the encapsulated NRs can be precisely tuned in a "dose-dependent" manner. The LSPR band becomes slightly spectrally narrower after irradiation which is caused by spectral hole burning. However, the TSPR peak is weakened, which indicates that the AuNRs are not converted into spheres and that some damping of the TSPR band occurs due to diameter heterogeneity, and enhanced surface scattering from the roughness.

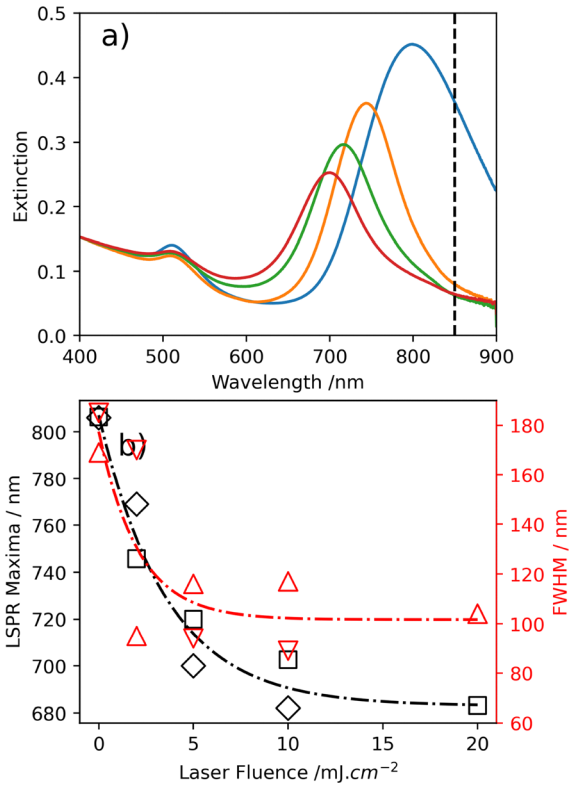


Fig. 6 The UV-vis-NIR extinction spectrum (a) of the AuNRs@$SiO_2$ samples before (solid blue line) and after 5 min of irradiation at a fluence of 20, 10, 5, and 2 mJ cm$^{-2}$ which are represented by orange, green, red, and purple curves, respectively. The vertical dashed line indicates the wavelength of the nanosecond pulsed laser source (850 nm). The spectra have been normalized to the extinction at 400 nm. (b) The LSPR maxima (black squares and diamonds) and the LSPR full-width-half-maximum (red triangles) of two independent experiments are plotted against laser fluence. The black dot-dashed line is a line of best fit to an exponential decay function. The red dash-dot line is a line of best fit through these FWHM data with an exponential decay function.

STEM images of the AuNRs exposed to 5 mJ cm$^{-2}$ ($\lambda$ = 850 nm) results in similar reshaping as the irradiation closer to the plasmon maxima, but with a smaller cavity (Fig. 7). The AuNRs are reshaped and many of the cores can be characterized as dumbbell shaped within the silica shell. There are some of the Au core nanorods that no longer have shells.

Quantitative analysis of the post-irradiation size distributions provides further insight into the off-resonance reshaping mechanism (Fig. 8). As expected, the TEM data show a clear decrease in the mean length (Fig. 8a) and a corresponding increase in the mean diameter (Fig. 8b) of the Au cores. This geometric shift resulted in a population with a lower average *AR*. The TEM size analysis does not show evidence of *AR* distribution narrowing. The end cap geometry does shifts from an oblate hemispherical cap to almost spherical ($e$ = 0.7 to $e$ = 0.9), with a narrower distribution (Fig. S18 in the SI). To directly probe the crystallographic changes induced by pulsed laser irradiation, a STEM capable of spatially mapping electron diffraction patterns was used to characterize AuNR samples (4D-STEM). The resulting diffraction patterns were indexed to

 

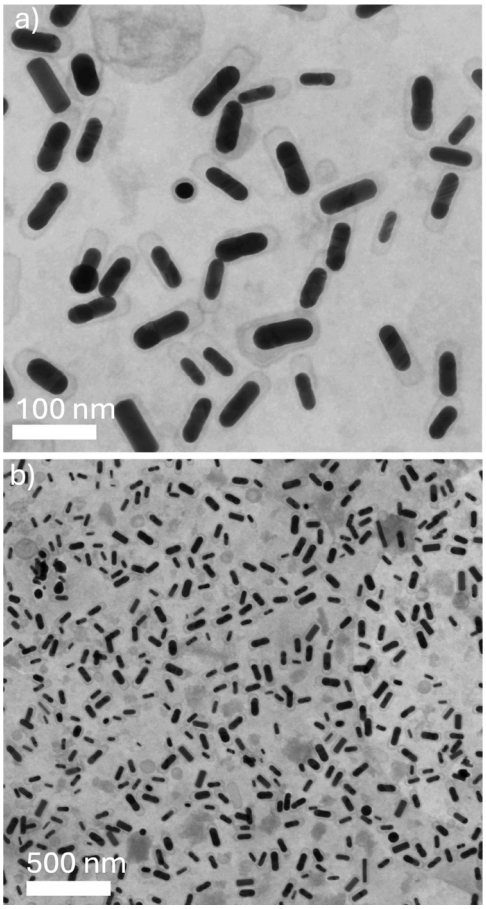


Fig. 7 High-resolution (a) and low-resolution (b) brightfield STEM images of the AuNRs@$SiO_2$ particles after 5 min of 5 mJ $cm^{-2}$ nanosecond-pulsed laser irradiation using a wavelength of 850 nm.

the fcc crystal structure of Au and visualized using inverse pole figure (IPF) maps to reveal the orientations of the crystal individual AuNRs (Fig. 9). Before irradiation, the AuNRs@CTAB were confirmed to be single crystals (Fig. 9a–d). The IPF maps show a uniform color across each individual AuNR, indicating that the entire particle is oriented along a single crystallographic zone axis, consistent with a defect-free, monocrystalline structure.

In contrast, after 5 min of irradiation at 5 mJ $cm^{-2}$, both AuNRs@CTAB and AuNRs@$SiO_2$ samples became polycrystalline. The IPF maps for these samples reveal multiple crystal orientations within a single particle, visualized by multiple color domains (Fig. 9g–m). This confirms that laser-induced heating causes complete melting and recrystallization of the Au core. The AuNRs@CTAB particles reshaped into more spherical forms (consistent with Fig. 3c) and exhibited large grain boundaries characteristic of a polycrystalline nanomaterial (Fig. 9f and h). The AuNRs@$SiO_2$ samples preserved their rod-like morphology, though the cores developed significant internal defects, including twin boundaries (Fig. 9j–l). This confirms that the Au cores of the AuNRs@$SiO_2$ particles have melted and recrystallized with multiple nucleating sites, which occur in different locations of each core.

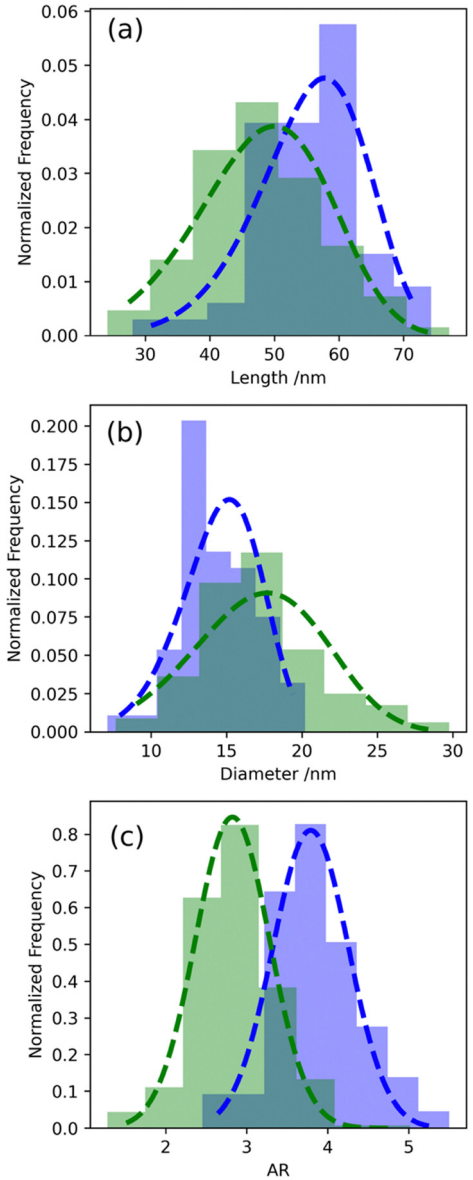


Fig. 8 Histograms of the AuNR core geometry of the shorter *AR* AuNRs@$SiO_2$ particles (d f) samples before (blue) and after (green) 5 min of pulsed irradiation with a fluence of 5 mJ $cm^{-2}$ ($\lambda$ = 850 nm). The histograms of the AuNR core diameters, *D* (a); lengths, *L* (b); and aspect ratios, *AR* (c). The dashed lines are the corresponding fits to Weibull distribution functions ($N > 100$).

## 4. Discussion

The binary surfactant method successfully produced AuNRs with a LSPR peak in the near-infrared and a TSPR peak at 511 nm, consistent with previous work.[32,33] The AuNRs exhibited approximately hemispherical end-caps. This cap geometry is known to influence the LSPR peak position but has a negligible effect on its FWHM.[38,41,42] Coating the AuNRs with a silica shell induced a slight redshift in both the LSPR and TSPR peaks, which is attributed to the increased refractive index of the medium immediately surrounding the Au core. The silica shells were uniform, following the rod-like shape of

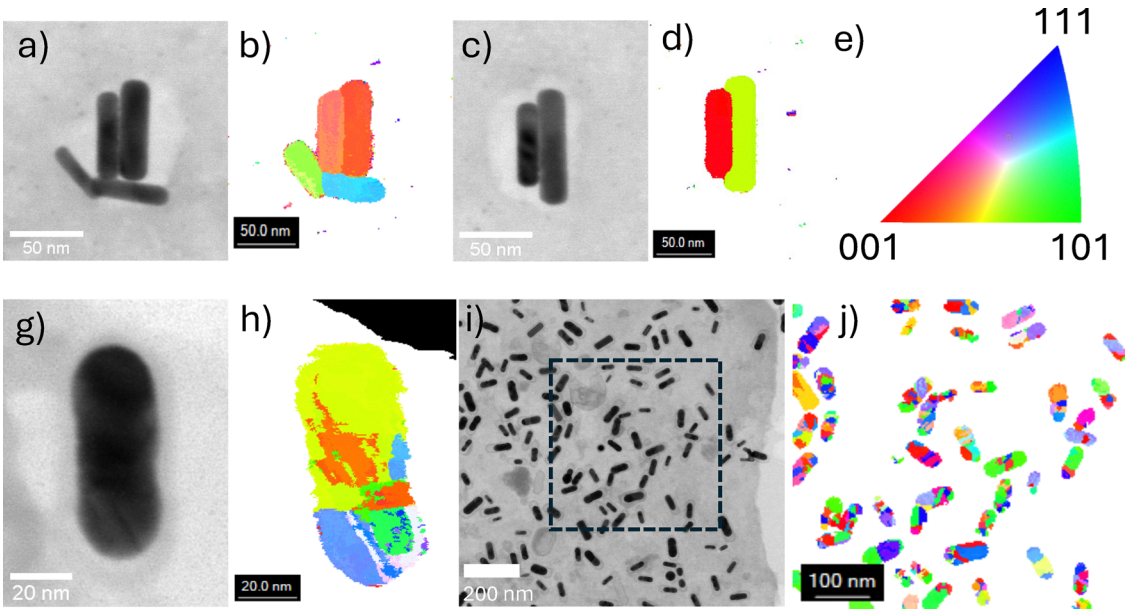


Fig. 9 Crystallographic analysis of AuNRs before and after laser-induced reshaping using 4D-STEM. Brightfield STEM images are paired with corresponding crystal orientation maps. The colors in the maps represent the out-of-plane (*z*-axis) crystallographic orientation, derived from electron diffraction patterns and indexed according to the fcc Au Inverse Pole Figure (IPF) key shown in (e). (a)–(d) Two representative images of AuNRs@CTAB nanorods before irradiation. The uniform color in the orientation maps (b) and (d) confirms their initial monocrystalline structure. (e) The reference IPF color key for fcc Au. (f)–(i) AuNRs@CTAB particles after 5 min of irradiation at 5 mJ $cm^{-2}$ ($\lambda$ = 850 nm). The particles have reshaped, and the orientation maps (g) and (i) reveal multiple color domains, indicating a transformation to a polycrystalline state. (j) and (k) High-magnification of a single AuNRs@$SiO_2$ particle after irradiation and showing the development of polycrystalline domains. (l) and (m) A lower-magnification overview of multiple irradiated AuNRs@$SiO_2$ particles. The orientation map (m), corresponding to the boxed region in (l), confirms that all the reshaped cores have become polycrystalline.

the core with a mean thickness of 6.8 nm and an average porosity of ~43%. The presence of a CTAB layer on the Au surface, confirmed by EDX, was found to be essential for maintaining colloidal stability during the silica growth process.

Upon irradiation with a nanosecond-pulsed laser tuned to the LSPR, the shelled (AuNRs@$SiO_2$) and unshelled (AuNRs@CTAB) particles exhibited distinctly different reshaping behaviors. During laser exposure, the LSPR of the unshelled AuNRs@CTAB was rapidly extinguished, accompanied by a corresponding increase in the TSPR band. This spectral change is consistent with the observed morphological transformation into spherical and ϕ-shaped nanoparticles.[15] In contrast, the AuNRs@$SiO_2$ samples underwent a more controlled transformation. The LSPR peak blue-shifted from ~830 nm to ~620 nm, indicating a decrease in the *AR* of the AuNR core. Crucially, the TSPR band did not increase in magnitude, confirming that the formation of spheres was suppressed by the shell. The incomplete disappearance of the original 830 nm peak suggests that the silica shell can, in some cases, effectively protect the AuNRs from major reshaping.

The observed reshaping is best explained by the complete melting of the Au core, followed by recrystallization. While simulations on smaller particles show a size-dependent shape transition temperature ($T_s$) before reaching complete melting, extrapolating these findings suggests a $T_s$ around 1000 K for the large particles used here, *i.e.* ~300 K below the bulk melting temperature.[21] Under the high-energy conditions of nanosecond laser pulses, complete melting within the shell is the dominant mechanism. When there is no shell present, the AuNRs become spherical, ellipsoidal, or ϕ-shaped. However, the presence of a shell confines the liquid Au and preserves a nanorod shape, albeit a reduced *AR* with irregular polycrystalline morphology. Importantly, once the LSPR of the core blueshifts past the laser wavelength, absorption ceases, and the reshaping is arrested. This process significantly narrows the FWHM of the LSPR band by ~60%. This optical finding aligns with reports of laser-induced monodispersity in unshelled AuNRs.[16]

The silica shell acts as a "nanocrucible" confining the molten Au and preventing it from collapsing into a sphere. This confinement often leads to the formation of a distinct dumbbell-like morphology, as the molten Au minimizes its Gibbs free energy by reducing its contact with the non-wetting silica surface (contact angle, $\theta_c > 130^\circ$) and beading up at the ends.[43] This dumbbell shape is the inverse of the ϕ-shape formed when unshelled AuNRs are irradiated.

A critical question is whether the shell provides sufficient volume for the core to decrease its *AR* and increase its width. TEM analysis confirms that the Au volume is conserved with no evidence of fragmentation. The necessary extra space is likely created by three possible processes: (1) localized etching of the porous silica shell (possible by superheated water[44]) (2), thermal decomposition of the ~3.2 nm thick organic CTAB-oleate layer,[45] or (3) the silica shell becomes denser during the heating.

 

The 4D-STEM analysis provides definitive evidence for the proposed mechanism. The AuNR cores transition from a monocrystalline state before irradiation to a highly polycrystalline state afterward, exhibiting numerous grain boundaries and twin defects. This confirms that the reshaping process involves a full melt-solidification cycle, where rapid heat dissipation during cooling prevents the formation of a perfect single crystal.

Finally, the reduction in the core *AR* reliably creates a nanocavity between the Au core and the silica shell, typically at one end of the rod. The size of this cavity can be controlled by adjusting laser fluence or irradiating at a wavelength above the LSPR. Compared to chemical etching methods, this laser-driven approach is a simple, rapid, and reproducible technique for fabricating nanocontainers.[30,31]

## 5. Conclusion

In conclusion, this study demonstrates a novel and straightforward method to controllably reshape AuNRs within a silica shell using nanosecond pulsed laser irradiation. This process reduces the core *AR* while preserving the overall rod-like morphology, creating a predictable nanocavity at one end. Unlike unshelled AuNRs which collapse into spheres, the confined cores retain their two characteristic plasmon bands, albeit with a significant blueshift LSPR. The 4D-STEM analysis provided definitive evidence for the underlying mechanism: the AuNRs undergo a monocrystalline-to-polycrystalline transformation, confirming that the core melts and rapidly recrystallizes within its shell. The melting and recrystallisation causes increased roughness and shape heterogeneity. This laser-driven technique offers a rapid route to fabricating AuNRs@$SiO_2$ nanocontainers. Future work should focus on scaling this method and exploring its potential in applications such as targeted drug delivery and nanoreactors.

## Author contributions

Conceptualization – KC; data curation - KC; formal analysis – TA, SA, LR; funding acquisition – KC; investigation – TA, SA, LR; methodology – JM, ZA; project administration – KC, SDE; supervision – KC, SDE, ZO; validation – TA, SA, LR, ZA; visualization – TA, SA, LR, KC; writing – original draft – TA, SA, LR, KC; writing – review & editing – all authors.

## Conflicts of interest

There are no conflicts to declare.

## Data availability

The data associated with this paper is available from University of Leeds at https://doi.org/10.5518/1787.[46]

Supplementary information (SI): additional experimental details and figures. See DOI: https://doi.org/10.1039/d6cp00240d.

## Acknowledgements

K. C. thanks the EPSRC (EP/T013753/1) for financial support. We thank BRG Johnson for technical support. L.R. acknowledges financial support from the Région Auvergne-Rhône–Alpes through the ''Amorçage Europe'' programme (No. 25 003102 01–15704). SA are thankful to the Deanship of Graduate Studies and Scientific Research at University of Bisha for the financial support through the Scholars Research Support Program.

## References

1 X. Huang, S. Neretina and M. A. El-Sayed, *Adv. Mater.*, 2009, **21**, 4880–4910.
2 J. Ma, Y. Li, Y. Ying, B. Wu, Y. Liu, J. Zhou and L. Hu, *Chem. Med. Chem.*, 2024, **19**, e202300374.
3 S. Si, A. G. Majumdar and P. S. Mohanty, *BioNanoSci.*, 2025, **15**, 185.
4 S. Link and M. A. El-Sayed, *Int. Rev. Phys. Chem.*, 2000, **19**, 409–453.
5 B. Nikoobakht, J. Wang and M. A. El-Sayed, *Chem. Phys. Lett.*, 2002, **366**, 17–23.
6 K. Ueno, S. Juodkazis, M. Mino, V. Mizeikis and H. Misawa, *J. Phys. Chem. C*, 2007, **111**, 4180–4184.
7 K. A. Willets and R. P. Van Duyne, *Annu. Rev. Phys. Chem.*, 2007, **58**, 267–297.
8 J. W. Cottom, P. Abellan, Q. M. Ramasse, K. Critchley and R. Brydson, *J. Phys. Chem. C*, 2018, **122**, 22041–22053.
9 J. Pérez-Juste, B. Rodríguez-González, P. Mulvaney and L. M. Liz-Marzán, *Adv. Funct. Mater.*, 2005, **15**, 1065–1071.
10 M. Das, N. Sanson, D. Fava and E. Kumacheva, *Langmuir*, 2007, **23**, 196–201.
11 Z. Zhang, Y. Wu, X. Cao, J. Gao, S. Yan, S. Su, Y. Wu, N. Zhou, X. Wang and L. Chen, *Nano Lett.*, 2024, **24**, 15127–15135.
12 X. Huang and M. A. El-Sayed, *J. Adv. Res.*, 2010, **1**, 13–28.
13 H. Takahashi, T. Niidome, A. Nariai, Y. Niidome and S. Yamada, *Chem. Lett.*, 2006, **35**, 500–501.
14 V. Amendola, R. Pilot, M. Frasconi, O. M. Maragò and M. A. Iatì, *J. Phys.: Cond. Matter*, 2017, **29**, 203002.
15 S. Link, C. Burda, B. Nikoobakht and M. A. El-Sayed, *J. Phys. Chem. B*, 2000, **104**, 6152–6163.
16 G. González-Rubio, P. Díaz-Núñez, A. Rivera, A. Prada, G. Tardajos, J. González-Izquierdo, L. Bañares, P. Llombart, L. G. Macdowell, M. Alcolea Palafox, L. M. Liz-Marzán, O. Peña-Rodríguez and A. Guerrero-Martínez, *Science*, 2017, **358**, 640–644.
17 S. M. Meyer, J. Pettine, D. J. Nesbitt and C. J. Murphy, *J. Phys. Chem. C*, 2021, **125**, 16268–16278.
18 C. Louis and O. Pluchery, *Gold Nanoparticles for Physics, Chemistry and Biology*, Imperial College Press, London, 2nd edn, 2011, ch. 4, DOI: 10.1142/p815.
19 K. Dick, T. Dhanasekaran, Z. Zhang and D. Meisel, *J. Am. Chem. Soc.*, 2002, **124**, 2312–2317.

20 S. J. Zhao, S. Q. Wang, D. Y. Cheng and H. Q. Ye, *J. Phys. Chem. B*, 2001, **105**, 12857–12860.
21 Y. Wang and C. Dellago, *J. Phys. Chem. B*, 2003, **107**, 9214–9219.
22 H. B. Liu, J. A. Ascencio, M. Perez-Alvarez and M. J. Yacaman, *Surf. Sci.*, 2001, **491**, 88–98.
23 J. Lyu, L. Matthews, T. Zinn, D. Alloyeau, C. Hamon and D. Constantin, *Nano Lett.*, 2025, **25**, 1544–1549.
24 M. Grzelczak and L. M. Liz-Marzán, *Chem. Soc. Rev.*, 2014, **43**, 2089–2097.
25 W. J. Kennedy, S. Izor, B. D. Anderson, G. Frank, V. Varshney and G. J. Ehlert, *ACS Appl. Mater. Interfaces*, 2018, **10**, 43865–43873.
26 A. Candreva, F. Parisi, G. Di Maio, F. Scarpelli, I. Aiello, N. Godbert and M. La Deda, *Gold Bull.*, 2022, **55**, 195–205.
27 M. Yaqub, G. A. Khan, H. Qayyum, M. A. Ghanem, A. Nadeem, Q. Abbas and W. Ahmed, *ChemistrySelect*, 2025, **10**, e00580.
28 V. A. Khanadeev, A. V. Simonenko, O. V. Grishin and N. G. Khlebtsov, *Nanomaterials*, 2023, **13**, 1312.
29 E. Choi, M. Kwak, B. Jang and Y. Piao, *Nanoscale*, 2013, **5**, 151–154.
30 Z. Li, J. Zhang, J. Jin, F. Yang, R. Aleisa and Y. Yin, *J. Am. Chem. Soc.*, 2021, **143**, 15791–15799.
31 Z. Wu, Y. Liang, Q. Guo, K. Zhang, S. Liang, L. Yang, Q. Xiao and D. Wang, *J. Mater. Sci.*, 2019, **54**, 8133–8147.
32 L. Roach, P. L. Coletta, K. Critchley and S. D. Evans, *J. Phys. Chem. C*, 2022, **126**, 3235–3243.
33 L. Roach, S. Ye, S. C. Moorcroft, K. Critchley, P. L. Coletta and S. D. Evans, *Nanotechnology*, 2018, **29**, 135601.
34 S. J. Ashrafi, F. Yazdian, A. S. H. Zaremi, J. Mohhamadnejad and R. Dinarvand, *Biomed. Pharma. J.*, 2016, **9**, 1189–1201.
35 P. A. Mercadal, L. A. Perez and E. A. Coronado, *J. Phys. Chem. C*, 2021, **125**, 15516–15526.
36 P. B. Johnson and R. W. Christy, *Phys. Rev. B*, 1972, **6**, 4370–4379.
37 L. Roach, *Synthesis, Functionalisation, and Biomedical Application of Phospholipid-Functionalised Gold Nanorods for Cancer Therapy*, PhD thesis, University of Leeds, 2019.
38 N. Xu, B. Bai, Q. Tan and G. Jin, *Opt. Express*, 2013, **21**, 21639–21650.
39 B. R. Jany, N. Gauquelin, T. Willhammar, M. Nikiel, K. H. W. van den Bos, A. Janas, K. Szajna, J. Verbeeck, S. Van Aert, G. Van Tendeloo and F. Krok, *Sci. Rep.*, 2017, **7**, 42420.
40 S. Wang, L. Fu, Y. Zhang, J. Wang and Z. Zhang, *J. Phys. Chem. C*, 2018, **122**, 24421.
41 Z. Hu, S. Hou, Y. Ji, T. Wen, W. Liu, H. Zhang, X. Shi, J. Yan and X. J. A. A. Wu, *AIP Adv.*, 2014, **4**, 117137.
42 N. Xu, B. Bai, Q. Tan and G. Jin, *Opt. Express*, 2013, **21**, 2987–3000.
43 E. Ricci and R. Novakovic, *Gold Bull.*, 2001, **34**, 41–49.
44 Z. Zhu, S. Zhang, C. Li, J. Zhang, J. Yu, X. Du, L. He and X. Zhang, *Phys. Chem. Chem. Phys.*, 2018, **20**, 1440–1446.
45 S. Gómez-Graña, F. Hubert, F. Testard, A. Guerrero-Martínez, I. Grillo, L. M. Liz-Marzán and O. Spalla, *Langmuir*, 2012, **28**, 1453–1459.
46 T. Albogami, R. Lucien, S. Alshehri, J. McLaughlan, Z. Aslam, Z. Ong, S. D. Evans and K. Critchley, Dataset of Photothermal Reshaping and Cavity Formation in Silica-Coated Gold Nanorods Using Nanosecond Pulsed Lasers, 2025, DOI: 10.5518/1787.

 